The Astrophysical Journal, 942:22 (14pp), 2023 January 1 https://doi.org/10.3847/1538-4357/aca324

Pre-main-sequence Brackett Emitters in the APOGEE DR17 Catalog: Line Strengths and Physical Properties of Accretion Columns

Hunter Campbell[1], Elliott Khilfeh[1], Kevin R. Covey[1], Marina Kounkel[1,2], Richard Ballantyne[1], Sabrina Corey[1], Carlos G. Román-Zúñiga[3], Jesús Hernández[3], Ezequiel Manzo Martínez[3], Karla Peña Ramírez[4], Alexandre Roman-Lopes[5], Keivan G. Stassun[2], Guy S. Stringfellow[6], Jura Borissova[7,8], S. Drew Chojnowski[9], Valeria Ramírez-Preciado[3], Jinyoung Serena Kim[10], Javier Serna[3], Amelia M. Stutz[11,12], Ricardo López-Valdivia[3], Genaro Suárez[13], Jason E. Ybarra[14], Penélope Longa-Peña[15], and José G. Fernández-Trincado[16]
[1] Department of Physics and Astronomy, Western Washington University, 516 High St., Bellingham, WA 98225, USA
[2] Department of Physics and Astronomy, Vanderbilt University, VU Station 1807, Nashville, TN 37235, USA
[3] Universidad Nacional Autónoma de México, Instituto de Astronomía, AP 106, Ensenada 22800, BC, México
[4] Centro de Astronomía (CITEVA), Universidad de Antofagasta, Av. Angamos 601, Antofagasta, Chile
[5] Departamento de Astronomia, Facultad de Ciencias, Universidad de La Serena, Av. Juan Cisternas 1200, La Serena, Chile
[6] Center for Astrophysics and Space Astronomy, Department of Astrophysical and Planetary Sciences, University of Colorado Boulder, Boulder, CO, 80309, USA
[7] Instituto de Física y Astronomía, Universidad de Valparaíso, Av. Gran Bretaña 1111, Playa Ancha, Casilla 5030, Chile
[8] Millennium Institute of Astrophysics, Nuncio Monsenor Sotero Sanz 100, Of. 104, Providencia, Santiago, Chile
[9] Department of Astronomy, New Mexico State University, Las Cruces, NM 88001, USA
[10] Steward Observatory, Department of Astronomy, University of Arizona, 933 North Cherry Av., Tucson, AZ 85721, USA
[11] Departamento de Astronomía, Universidad de Concepción, Casilla 160-C, Concepción, Chile
[12] Max-Planck-Institute for Astronomy, Königstuhl 17, D-69117 Heidelberg, Germany
[13] Department of Physics and Astronomy, The University of Western Ontario, 1151 Richmond St., London, ON, N6G 1N9, Canada
[14] Department of Physics and Astronomy, White Hall, Box 6315, West Virginia University, Morgantown, WV 26506-6315, USA
[15] Unidad de Astronomía, Universidad de Antofagasta, Avenida Angamos 601, Antofagasta 1270300, Chile
[16] Instituto de Astronomía, Universidad Católica del Norte, Av. Angamos 0610, Antofagasta, Chile
Received 2022 September 8; revised 2022 November 8; accepted 2022 November 10; published 2022 December 30

Abstract

Very young ($t \lesssim 10$ Myr) stars possess strong magnetic fields that channel ionized gas from the interiors of their circumstellar disks to the surface of the star. Upon impacting the stellar surface, the shocked gas recombines and emits hydrogen spectral lines. To characterize the density and temperature of the gas within these accretion streams, we measure equivalent widths of Brackett (Br) 11–20 emission lines detected in 1101 APOGEE spectra of 326 likely pre-main-sequence accretors. For sources with multiple observations, we measure median epoch-to-epoch line strength variations of 10% in Br11 and 20% in Br20. We also fit the measured line ratios to predictions of radiative transfer models by Kwan & Fischer. We find characteristic best-fit electron densities of $n_e = 10^{11}$–10^{12} cm^{-3}, and excitation temperatures that are inversely correlated with electron density (from $T \sim 5000$ K for $n_e \sim 10^{12}$ cm^{-3} to $T \sim 12{,}500$ K at $n_e \sim 10^{11}$ cm^{-3}). These physical parameters are in good agreement with predictions from modeling of accretion streams that account for the hydrodynamics and radiative transfer within the accretion stream. We also present a supplementary catalog of line measurements from 9733 spectra of 4255 Brackett emission-line sources in the APOGEE Data Release 17 data set.

Unified Astronomy Thesaurus concepts: Accretion (14); Stellar accretion (1578); Pre-main sequence stars (1290); Be stars (142); Classical T Tauri stars (252); Emission line stars (460)

Supporting material: machine-readable table

1. Introduction

Early on, young stellar objects (YSOs) have massive protoplanetary disks through which they accrete gas. The material flows through the disk and, upon reaching the disk's inner edge, travels along the magnetic field lines onto the stellar surface (Hartmann et al. 2016). In the process, outflows are launched and remove excess angular momentum inherited from the rotating disk.

When this accreting material impacts the stellar photosphere, it forms a shock that emits both continuum and line emission from the heated and excited gas. Immediately following a particularly strong accretion event, the YSO may increase in brightness by several orders of magnitude, producing an FU Ori-type outburst (Bae et al. 2014). While typical accretion rates are significantly lower than in the one observed in these events to be sustainable over the lifetime of protoplanetary disks, even weak accretion signatures are nonetheless imprinted on the stellar spectra.

Most notable accretion signatures are reflected in the form of hydrogen emission lines, particularly Hα. Classical T Tauri stars (CTTSs) have wide Hα lines, with equivalent widths (EqWs) in excess of what is found in weak-lined T Tauri stars (WTTSs; White & Basri 2003). This is due to CTTSs having active ongoing accretion and outflows, whereas in WTTSs the emission is driven solely by the magnetic activity on the photosphere. In these WTTSs, the accretion is terminated and the protoplantary disks are largely depleted.

Hα is a particularly useful line to observe accretion because it is the lowest energy transition of hydrogen that is easily

observable, and it is easy to excite even with low accretion/outflow rates. However, other H lines, both higher-level lines in the Balmer series, as well as in other series, can also often be observed in emission in particularly active accretors. Through using multiple transitions it is possible to determine the properties of the infalling gas, such as its temperature and density (Kwan & Fischer 2011; Antoniucci et al. 2017; Gutiérrez et al. 2020). In turn, the bulk census of sources for which these parameters are known yields better constraints on the accretion models of YSOs.

In this paper, we use APOGEE spectra to identify sources with Brackett (Br) emission lines that fall in its spectral range in the *H* band, 11 through 20. In Section 2.1 we describe the data used for this analysis. In Section 2.2 we measure the EqWs of these lines. Then, in Section 3.2 we perform model fitting to these measurements to constrain the properties of the gas that is responsible for the emission. In Section 4 we discuss the results, and in Section 5 we offer the conclusions.

2. Data and Methods

2.1. Observations

We analyze high-resolution ($R \sim 22{,}500$) near-IR (NIR; 1.51–1.70 μm) spectra taken with the 300-fiber APOGEE spectrograph (Wilson et al. 2019) on the Sloan 2.5 m telescope (Gunn et al. 2006) at Apache Point and Las Campanas Observatories. To generate a comprehensive, uniform, and complete catalog of Brackett emission sources, we process the full contents of the Sloan Digital Sky Survey (SDSS)-IV Data Release 17 (Abdurro'uf et al. 2022). The APOGEE Data Release 17 (DR17) data set includes all previously released APOGEE and APOGEE-2 spectra; in total, the data set contains 2,659,178 individual spectra, all of which have been re-reduced with the latest version of the APOGEE data-reduction and analysis pipeline (Holtzman et al. 2015; Nidever et al. 2015; García Pérez et al. 2016; Jönsson et al. 2020; J. Holtzman et al. 2022, in preparation).

Brackett emitters should be relatively rare in this data set, however, as most stars targeted by APOGEE are red giants, whose luminosity makes them a superb tracer for dissecting the structure, dynamics, chemical evolution, and star formation history of the Milky Way (Majewski et al. 2017). The APOGEE-2 footprint is designed to sample these red giants along systematic tiling of sight lines through the Galaxy's bulge, disk, and halo (Zasowski et al. 2013; Blanton et al. 2017; Zasowski et al. 2017), but Brackett emitters, particularly the bona fide accreting YSOs which are of most scientific interest in this paper, are concentrated in a small number of plates that overlap nearby star-forming regions. Some standard APOGEE and APOGEE-2 plates may overlap with these star-forming regions serendipitously, and can be identified in the survey tiling maps presented by Santana et al. (2021) and Beaton et al. (2021) in their summaries of the final targeting strategies for the southern and northern APOGEE programs, respectively. We expect the vast majority of the bona fide accreting YSOs to be identified outside of the standard survey tiling, however, on plates observed as part of the APOGEE-1 IN-SYNC ancillary program (Cottaar et al. 2014; Foster et al. 2015; Da Rio et al. 2016), the APOGEE-2 Young Cluster Survey (Cottle et al. 2018; Kounkel et al. 2018; Román-Zúñiga et al. 2022), or through several APOGEE-2 contributing programs targeting other star-forming regions (e.g., Borissova et al. 2019; Roman-Lopes et al. 2020; Medina et al. 2021). We tabulate in Table 1 the specific set of young cluster plates upon which we focus our search and analysis efforts.

Table 1
Young Cluster Plates

Region	Plates	N_{Br}[a]
IC 348	6218–6223, 7073–7075, 7079, 10100, 12706	12
NGC 1333	6224–6226, 7070–7072, 11425	7
NGC 2264	6103, 6227, 10302, 11778	17
Orion-A	7220–7234, 9481, 9533, 9659–9661, 11593–11594, 12273	98
Orion-B	8890–8899	19
Orion-OB1ab	8900–8906, 9468–9480	14
Lambda Ori	8879–8887, 9482, 9537, 9538	6
Pleiades	8889, 9257	0
Taurus	9258–9259, 9287–9288, 11426–11431	8
Cor-Aus	10718	0
Vela Ridge	12276	7
Rosette	11440–11441, 12266	2
H and χ Persei	9244	5
California Neb.	11432–11438	6
Carina	9752, 10294–10298, 11620–11622, 12356–12358	56
Cygnus X	11271–11276, 11409–11420	69

Note.
[a] Number of sources with detectable Br11 emission in a given region, excluding double-peaked or nebular sources.

2.2. Line and Line Ratio Measurements

2.2.1. Spectral Preparation

To prepare the spectra for EqW and line ratio measurements, we clean them of cosmetic artifacts (i.e., chip gaps and sky line residuals) that can contaminate the line or continuum regions used in our measurements, and then place each spectrum in a consistent barycentric velocity frame. We do not attempt to correct to the rest frame of the pre-main-sequence star, however, as the strong emission lines within the spectrum often degrade the quality of the radial velocity measurement of the individual visits produced by the APOGEE pipeline.

We use individual visit spectra in our analysis to preserve information about variations in the strength or velocity profile of the Brackett lines. The spectra in the apVisit files are presented in the observed, geocentric velocity frame. We mask regions associated with prominent telluric emission lines to eliminate any residuals that may be left in the spectrum. For this process, we utilize the line list of telluric features in the APOGEE bandpass first used by Cañas et al. (2018) to mask APOGEE spectra of Kepler 503-b prior to radial velocity measurement.

APOGEE spectra are recorded using three distinct detectors, each covering a different range of wavelengths (red, green, blue). The cutoffs between the detectors occur near the Br12 and Br15 lines. Depending on the velocity of the source, these spectral gaps can fall within the continuum regions used to measure the Br12 and Br15 EqWs. We therefore interpolate

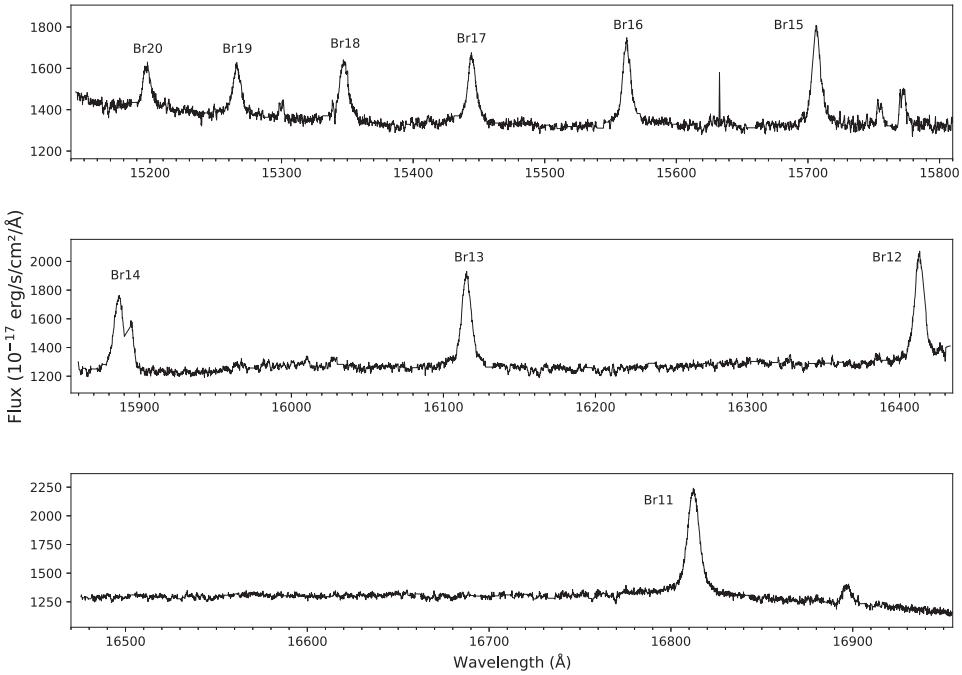

Figure 1. Full spectrum plot of the Br11–20 emission lines for a strongly accreting YSO, 2M05471411+0009073.

over the wavelengths that fall in the gaps between detectors, using the mean values of the pixels on either edge. However, we independently estimate the signal-to-noise ratio (S/N) for each detector for each observation.

To determine the wavelength correction required to place these spectra in the barycentric frame, we used the pyAstronomy `helcorr` package[17] (Czesla et al. 2019) to calculate the barycentric correction, based on the original IDL implementation by Piskunov & Valenti (2002). This function uses the target coordinates and the time and location of observation. We adopt the following longitude, latitude, and elevations for each site: APO—long. = −105.°4913, lat. = 36.°4649, elevation = 2788 m; LCO—long. = −70.°413336, lat. = −29.°05256, elevation = 2380 m.

Figure 1 shows a final corrected spectrum for 2M05471411 +0009073, a sample YSO with strong Brackett emission lines.

2.2.2. Line Measurement

To measure the EqWs of the Brackett 11–20 lines, we defined windows centered on each line's rest wavelength from which to measure the line flux. These windows are defined to be 240 spectral elements (i.e., pixels) in width, such that they typically contain the full width of each Brackett emission line, regardless of the radial velocity of the star. We then measure the continuum for each line as the median flux of two windows of 121 spectral elements on either side of this line region. Figure 2(a) highlights these continuum regions with green shading, on either side of the line region for a strong Brackett 11 (which we abbreviate hereafter as Br11) emission line. We measure the pure emission component by subtracting the interpolated continuum flux from the flux in the main line window; integrating the residuals and dividing by the continuum flux provides our EqW measurement in units of angstrom.

[17] See https://pyastronomy.readthedocs.io/en/latest/pyaslDoc/aslDoc/baryvel.html#PyAstronomy.pyasl.helcorr and https://github.com/sczesla/PyAstronomy.

We calculate uncertainties for these EqW measurements using the formalism of Vollmann & Eversberg (2006), as validated by a comparison to the observed variance of line measurements for sources with multiple observations. The Vollmann & Eversberg (2006) formalism allows the uncertainty in an EqW measurement to be calculated as

$$\sigma(W_\lambda) = \sqrt{1 + \frac{\bar{F}_c}{\bar{F}}}\,\frac{(\Delta\lambda - W_\lambda)}{S/N}, \quad (1)$$

where $\bar{F}_c$ and $\bar{F}$ are the mean flux in the continuum and line regions, respectively, while W_λ, $\Delta\lambda$, and S/N are the EqW, actual width, and mean S/N of the line in question. Of these values, all but the line's actual width are calculated automatically during the EqW measurement. The line's actual width is more difficult to measure in an automated fashion, so we approximate $\Delta\lambda$ as the full width of our line measurement window. As typical lines only span half to a third of the line measurement window, this will bias our error estimates toward somewhat larger values than would be calculated with a line-by-line width measurement. The Br11–20 lines share a similar width across the full decrement, however, as the width is largely set by the Doppler broadening imposed by the velocity structure of the accretion stream. As a result, while the line-by-line uncertainties will likely be overestimated by a factor of ∼2, this overestimate will not bias the chi-square minimization we perform in Section 3.2.2, but instead will simply adjust the zero point of the chi-square minimization process.

3. Results

3.1. Catalog

3.1.1. Catalog Construction

We consider spectra to have significant emission if Br11 EqW > 0.75 Å (Figure 2(b)), and a ratio of the measured EqW

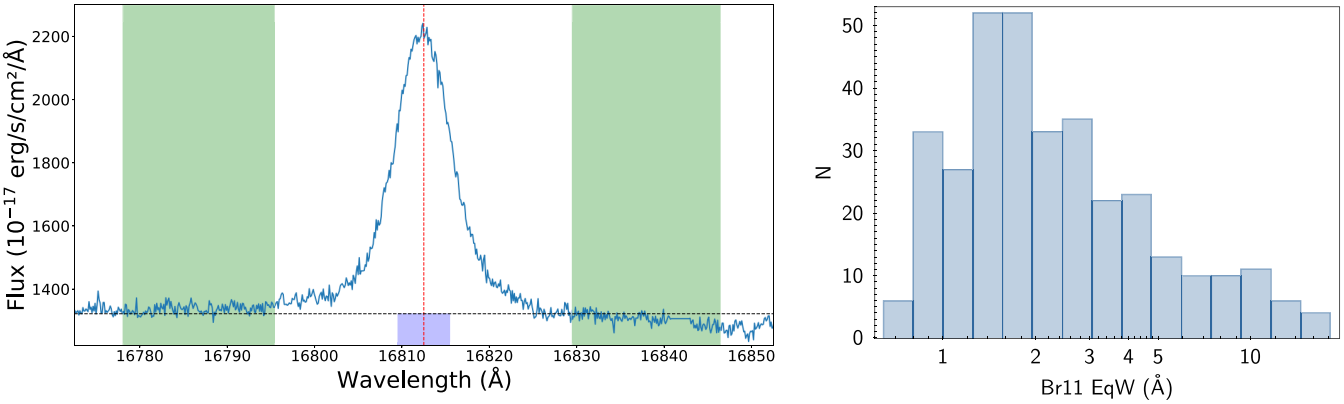

Figure 2. Left: wavelength–flux plot of the Br11 emission line for a strongly accreting YSO, 2M05471411+0009073. The green highlighted regions are the windows which were used to calculate the continuum (horizontal dashed line) on the left and right of the central line (vertical dashed line). The equivalent width (EqW) of the Br11 line is given by the width of the shaded blue region below the continuum. Right: distribution of the absolute value of EqWs for Br11 for all of the objects in the sample, excluding those that are likely associated with Be stars or that have nebular emission. Note that since the Br11 line is seen in emission, by convention the EqW is negative.

to the estimated uncertainty of greater than 1. Restricting our attention to spectra obtained with the young cluster plates listed in Table 1, we identify 3195 spectra of 879 sources that meet these criteria for a significant Br11 emission line. We report the line measurements, and their errors, for these sources in a machine-readable .csv file, whose columns are documented in Table 2.[18] Expanding our search to all spectra in DR17, we find 9733 visit spectra corresponding to 4255 unique sources satisfying such a criterion. We present EqW measurements for these sources in a machine-readable table, whose columns are documented in Table 2, as well, but the processes producing these Brackett emission lines are much less likely to be related to pre-main-sequence magnetospheric accretion. Be stars, for example, are known to exhibit APOGEE spectra with prominent, but often double-peaked, Brackett emission lines (e.g., Chojnowski et al. 2015); we also detect a number of spectra with narrow (full width <200 km s^{-1}) Brackett emission lines in known H2 regions, which we classify as likely nebular sources. As a result, we do not analyze this larger catalog directly, but use it instead as a resource to refine our sample of bona fide YSO emission-line sources, by making manual measurements for a subset of the broader catalog and then training a neural network to identify likely Be stars or nebular emission lines based on the morphology of their Brackett emission-line profiles.

3.1.2. Machine Learning

To further remove contaminants in an automatic way, and provide more accurate estimates of the line profile parameters such as the line width and single/double peak status, we constructed and trained a neural network using a training set constructed from visual examination of a random subset of 500 spectra of Brackett-emitting candidates. In examining it, we have flagged lines that did not have Brackett emission, or lines that appeared to be double-peaked (such emission most likely originates from Be stars, Chojnowski et al. 2015). For the lines that did have Brackett emission, we manually measured EqW using a custom interactive interface through specifying the apparent full width of the line and the continuum. We also estimated the central velocity of the line. Four people have performed independent manual measurements for the same set of 500 spectra, to characterize systematic differences in the placement of the continuum.[19]

Afterwards, we constructed a neural network to automate the classification. The training set consisted of the 80 Å cutout of the APOGEE spectra around all Br11–20 lines, centered on the rest wavelength of each line. To minimize the noise and optimize the training process, these spectral windows have been rebinned to 0.25 Å resolution, such that each spectral window consisted of 320 separate data points. To prevent the model from basing all of its predictions for a given spectrum just on the strongest Br11 line, each line in each spectrum was treated separately, as were all four independent manual measurements for each line. Thus, the set has consisted of 20,000 spectral windows, consisting of logFlux to bring the data to a more narrow range of inputs. In total, 80% of this set was used for training and 20% has been withheld as a validation sample.

The neural network model was constructed using TensorFlow (Abadi et al. 2015), consisting of four convolutional layers and four fully connected layers, with layers connected with the tanh activation function. Two separate tasks were performed. First, classification, providing a probability that a given spectral window had one of three flags: (1) an emission line is present in the spectrum, (2) an emission line is present but it appears to be double-peaked, and (3) there is no emission line in the spectral window. The probability of all three would add up to 100% for each line.

Following the classification, a separate network with a similar architecture performed regression tasks. For the spectral windows with a detected line, it would estimate the log EqW, log full width, and log wavelength offset to the line center.

Sparse categorical cross-entropy loss was minimized for training the classification model, and mean squared error loss

[18] We do null Br12–20 line measurements for four young cluster targets whose line measurements produce spuriously high line or uncertainty values: 2M03423420+3151008, 2M04541715+3142224, 2M05011102+3114125, and 2M10450433-5957352. We also null the uncertainty of the automated Br12 line measurement of one source, 2M20231719+3923587, whose Br12 EqW is larger than the width of the measurement window, such that the formalism in Equation (1) produces a negative uncertainty.

[19] In the course of the visual analysis to manually measure line strengths for this training set, we identified 63 sources with emission lines blueward of their Br11 line. We show examples of these spectra in Appendix, and include an "Fe II" column in the main machine-readable table to highlight these sources, coded with flags of 1, 2, and 3, respectively.

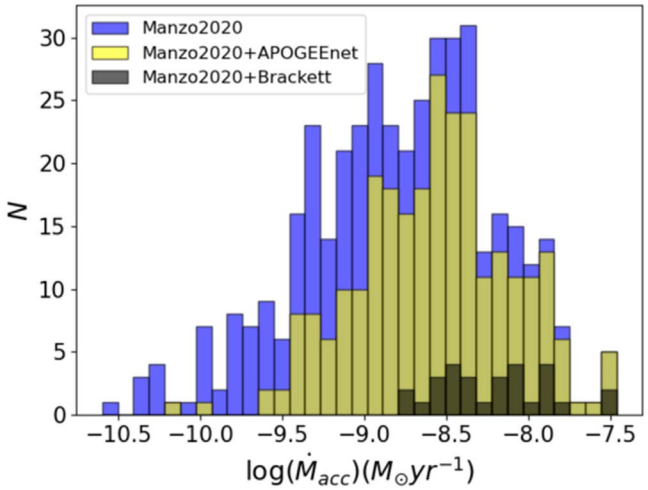

Figure 3. Accretion rate measurements for sources with optical measurements by Manzo-Martínez et al. (2020; full sample shown as the blue histogram), highlighting the subsets of sources with APOGEEnet stellar parameters (yellow histogram), and with Brackett emission lines detected in this work (black histogram). The Brackett sample is strongly biased toward the most rapidly accreting sources in the Manzo-Martínez et al. (2020) sample, given the larger temperatures and densities required to populate hydrogen's $n = 11$–20 levels, and the larger optical depths that are necessary to produce detectable emission lines.

was used for the regression model. Both models used an Adam optimizer with a learning rate of 1×10^{-4}. The training was continued until the loss in the validation sample did not improve for 20 epochs.

After applying the trained model on all spectra identified in Section 3.1.1, we identify the bona fide emission lines. Leveraging all of the model predictions for all the lines, we identify the maximum Brackett line that is detectable in the spectrum. Since the line profile should be very similar for all of the detected lines, we average the classification to identify double-peaked sources. We similarly estimate the Doppler shifts for all of the lines, as well as the typical width of the line in units of kilometers per second. Based on the width of the line profile, we also identify sources most likely to be nebular in origin: such sources tend to have narrow lines with an average full width <250 km s^{-1} and Br11 width <13 Å. In contrast, emission lines for the accreting young stars tend to have a full width of ∼300–400 Å, and double-peaked Be stars tend to have full width of ∼800 Å.

As noted earlier, our automated EqW measurements identify Br11 emission features in 3195 spectra of 879 unique sources on the young cluster plates listed in Table 1. Our trained neural network independently confirms the emission lines detected for ∼98% of these spectra (3136/3195) and sources (858/895). Of these confirmed emitters, however, the network classifies nearly a third as having line profiles consistent with a Be star classification (1256 spectra of 299 sources) or a spectrum with nebular emission features (779 spectra of 282 sources). The remainder, consisting of 1101 spectra of 326 sources, exhibit single-peaked emission profiles with velocity widths consistent with magnetospheric accretion. Together with their angular proximity to known star-forming regions and young clusters, we identify these sources as likely accreting pre-main-sequence stars, and proceed to analyze their line strengths to infer the temperatures and densities of their accretion flows.

We report these neural network classification results in a machine-readable table, whose columns are documented in Table 2.

3.1.3. Comparison to Optical Accretion Rate Estimates

To quantify typical mass-accretion rates for pre-main-sequence stars with robustly detected Brackett emission lines, we analyze accretion rate measurements reported by Manzo-Martínez et al. (2020) based on analysis of optical Hα line measurements for 835 T Tauri stars in the ONC, σ Ori, Orion OB1a/b, and Taurus. The full sample of 420 optically derived accretion rates measured by Manzo-Martínez et al. (2020) are shown in Figure 3, with histograms overlaid to highlight the 268 sources with optically derived mass-accretion rates for which APOGEEnet spectral parameters (and thus APOGEE spectra) are available, and the much smaller set of 30 sources for which a Br11 emission line has been detected. As Figure 3 demonstrates, we only detect Br11 emission for ∼11% of the 268 stars with APOGEE spectra and accretion rates measured by Manzo-Martínez et al. (2020). The sources in the Manzo-Martínez et al. (2020) sample with Br11 detections are also strongly biased toward higher mass-accretion rates: their optically derived mass-accretion rates all exceed the median rate measured by Manzo-Martínez et al. (2020) of 1.6×10^{-9} $M_\odot$ yr^{-1}.

Figure 3 also demonstrates, however, that while all pre-main-sequence stars with well-detected Brackett emission lines have high optically derived accretion rates, the inverse does not hold: we do not detect Brackett emission lines from all sources with APOGEE spectra and large optically inferred accretion rates. Of the 268 sources with both APOGEE spectra available and accretion rate estimates by Manzo-Martínez et al. (2020), 179 (or more than two-thirds) have an optically derived accretion rate larger than the smallest accretion rate measured for the 30 sources with Br11 detections. Put another way, we only detect Br11 emission for one-sixth of the sources with accretion rates higher than the lowest Br11 detection: five-sixths of these high-accretion-rate sources are null detections for our Brackett analysis. To better understand the nature of the sources with strong Hα-derived accretion rates but no detected Brackett emission lines, we visually inspected all APOGEE spectra available for the 30 sources with the highest optical accretion rate measurements in the Manzo-Martínez et al. (2020) sample, but which were not identified as strong accretors in the Brackett emission sample. APOGEE spectra are available for 24 of these 30 high-accretion-rate sources, but none have Brackett line detections reported in a machine-readable table, whose columns are documented in Table 2. Visual inspection confirms a lack of reliable Brackett line emission in the APOGEE spectra of these 24 sources, particularly in the Br11 line used to select sources with robust emission detections. Three sources (2M05343822-0524236, 2M05345292-0528591, and 2M05352463-0519096) appear to exhibit Br11 emission just below the detection limit of our catalog, but their Br11 EqWs and/or S/N estimates do lie just outside the bounds of our detection limit, such that the Br11 emission feature must be considered as marginal rather than secure. We comment more on the astrophysical implications of the disconnect between these optical and NIR accretion indicators in Section 4.1, limiting the discussion here to verifying and documenting the lack of agreement between Balmer- and Brackett-selected accretors.

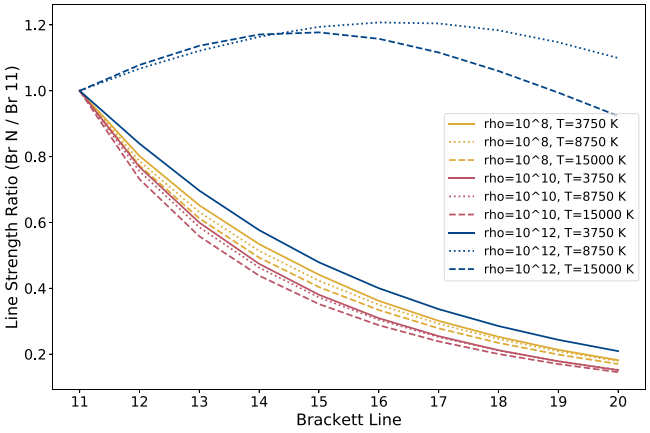

Figure 4. Kwan & Fischer (2011) model grid, showing the decrement of the emission in Brackett lines relative to the Br11 line, separated into a range of different temperatures and densities of the emitting gas. Note that the most distinct decrement models have high density and high temperature.

3.2. Model Fits

3.2.1. Kwan and Fischer Line Strength Calculations

Kwan & Fischer (2011) performed detailed local excitation calculations to determine the emissivity ratios of hydrogen lines in the Balmer, Paschen, and Brackett series. Unlike prior work, which makes strong assumptions about the optical thickness and level populations of the line ratios in question (e.g., the Case B recombination models calculated by Baker & Menzel 1938 and Hummer & Storey 1987), Kwan & Fischer (2011) calculate the radiative and collisional equilbria for each set of input parameters, and calculate level populations and emissivities in a self-consistent manner. These calculations were performed assuming a nominal UV excitation field, over a range of temperatures ($5000 < T < 30{,}000$ K) and hydrogen nucleon number densities ($10^8 < n_{\rm H} < 2\times10^{12}$ cm^{-3}) relevant for gas in protostellar accretion flows. In their initial work, Kwan & Fischer (2011) reported emissivity ratios for hydrogen lines up to $n = 15$; as APOGEE spectra sample transitions up to the Br20 line, additional calculations of the emissivity ratios of these higher-order transitions were kindly provided by J. Kwan & W. Fischer (2015, private communication) for the same grid of temperatures and densities as in their 2011 publication.[20]

The relative line strengths predicted for a sparse, grid-spanning set of temperatures and densities are displayed in Figure 4. For each model, all line strengths are normalized by the observed strength of the Br11 line; we refer to a set of such normalized line strengths, either in our model grid or as measured from an empirical spectrum, as a Brackett decrement. At lower densities (i.e., $n_{\rm H} \sim 10^8$ and 10^{10}), the Brackett lines are optically thin, and the decrement is only marginally sensitive to the gas temperature. As such, even moderate observational errors may significantly affect the confidence of the temperature determinations for any targets whose decrement is consistent with a lower-density fit. The decrements predicted for higher-density models are significantly more temperature sensitive, however, and populate a much more unique area of line ratio parameter space. As a result, in the absence of substantial observational errors, any fits that return a higher density will also provide a much more precise constraint on the temperature of the emission region.

3.2.2. Calculating and Fitting Empirical Brackett Decrements

Once we calculated the EqWs of the Brackett 11–20 lines for each spectrum, we took the ratio of each spectrum's line EqW to their respective Br11 EqW to measure the decrement in line strengths from Br11 to Br20. We then compared these measured decrements to the predictions by Kwan & Fischer (2011) for the 161 temperature and density points in their model grid. This grid spans densities from 10^8 to $10^{12.4}$ cm^{-3} and temperatures from 3750 to 15,000 K.

It is important to note that the decrements we construct from continuum-normalized EqW measurements are not fully equivalent to the flux-weighted intensity ratios predicted by the Kwan & Fischer (2011) model grid. Producing astrophysically accurate intensity ratios would require not only flux-calibrated spectra, which APOGEE provides, but also accurate corrections for the effects of foreground extinction on both the line and continuum flux. As the line flux and continuum sample different emission regions (i.e., the accretion column and stellar photosphere, respectively), determining a robust extinction likely requires detailed modeling of the circumstellar environment. We have estimated the uncertainties associated with fitting Brackett decrements based on EqW measurements rather than extinction-corrected line fluxes, however, by examining the range of spectral slopes in our sample and the additional wavelength dependence imposed by uncorrected foreground extinction. The median spectral slope in our YSO sample, measured as the ratio of the continuum fluxes for the Br11 to Br20, is 0.9, with 10% and 90% deciles of 0.78 and 1.16, respectively. That is, our median EqW-based Br20/Br11 line strength ratio is underestimated relative to the intensity-weighted ratio by 10% (i.e., a measured EqW ratio of 0.2 would correspond to an intensity-based ratio of 0.22). This bias scales with the wavelength separation of the lines in question, so will be lesser for line ratios that have smaller separations (i.e., the bias in the Br13/Br11 ratio should only be half as large), and is typically a factor 2–3 lower than the uncertainties in our line ratios.

The uncertainty in our EqW-based line ratios due to neglecting effects of extinction is harder to scope. Extinction of $A_V = 1.5$ will skew the continuum slope across the APOGEE spectrum of a $T \sim 4000$ K source by about 4%. If the line formation region and the stellar photosphere have the same foreground extinction, however, neglecting this correction should not affect the accuracy of our EqW-based line ratios, as both the line and continuum regions will be equally extinguished, and the the EqW ratio will correspond directly to the intensity-weighted ratio. However, it is not obvious that the Brackett line formation region, which likely samples some of the accretion column as well as the accretion shock, will have the same line-of-sight extinction as the stellar-disk-averaged photospheric flux, which will dominate the continuum. Indeed, one might expect the photosphere to have a somewhat higher foreground extinction than the line formation region, such that the EqW-based ratios will be biased toward higher values than ratios based on intensities, as the continuum will be preferentially surpressed for the bluer lines in the decrement. Accounting for these extinction effects would likely require detailed modeling of the circumstellar environment of each source, as the geometry and temperature structure of the

[20] We note that the calculations for line ratios up to the $n = 20$ state of hydrogen are now publicly available at https://www.stsci.edu/~wfischer/line_models.html.

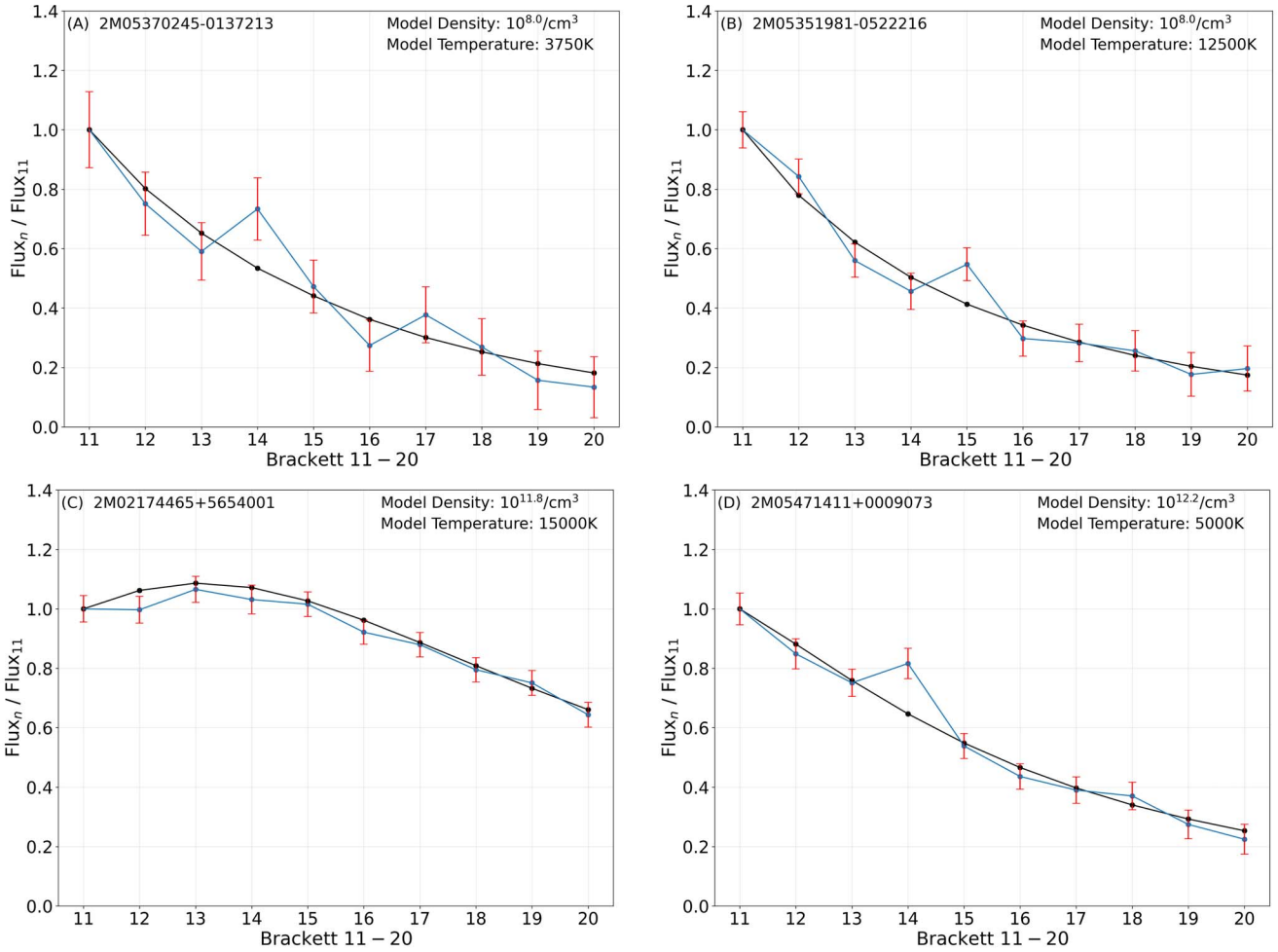

Figure 5. Sample decrement fits for several APOGEE spectra from the young cluster plates, ordered by density. Each spectrum shows a unique combination of model density and temperature values. The empirical decrement measured from the spectrum is shown as red data points, with empirical errors, while the best-fit model decrement is shown as a solid black line. Notes on the individual sources. (a) Br14 is located close to the chip gap, resulting in an uncertain estimate of the continuum. (b) Very narrow lines, likely nebular in origin; Br15 is affected by telluric subtraction. (c) Asymmetric double-peaked profile, likely a Be star. (d) Br14 appears to be affected by the blending with Si I 15892.771 line that is only rarely seen in emission.

circumstellar material will play a role in determining the amount of dust that is present along the line of sight to the different components that contribute to the spectrum.

Given the scale of these effects relative to our existing line measurement uncertainties, and the potential that the biases due to neglecting the measured spectral slopes and potential line-to-continuum extinction differences at least partially offset one another, we have not attempted to convert our EqW-based line ratios into astrophysically corrected intensity ratios. However, to allow the reader to assess the potential impact of performing these fits in EqW rather than intensity space, we include our Br20-to-Br11 spectral slope measurements in a machine-readable table, whose columns are documented in Table 2.

We used a least-squares regression to find the best density and temperature model for each spectrum. We calculated the total rms difference between the line strengths observed in each decrement and each model in our decrement grid, after normalizing each difference by the error associated with the measured line strengths, and then selected the model profile with the smallest total normalized difference as our best-fit model for that decrement. Two constants were added to the chi-squared calculations to create a minimum error in the normalized EqWs: a base, flat error of 0.01 to provide a minimum error level that accounts for effects whose precision does not scale cleanly with S/N, such as OH line subtraction and telluric absorption correction, and an error that scales with 2% of the ratio between the emission line and the Br11 EqW, to account for potential systematic errors that do not scale with S/N, such as the measurement of the stellar continuum.

These fit results are presented in a machine-readable table, whose columns are documented in Table 2. Best fit models are shown in Figure 5 for a representative set of spectra in our sample; similarly, Figure 6 shows a representative chi-square surface for the comparison of the line strengths of a single spectrum in our sample to the model predictions at every temperature and density in the Kwan & Fischer model grid.

3.2.3. Distribution of Best-fit Temperatures and Densities

Figure 7 shows the distribution of temperatures and densities identified from fitting the theoretical Brackett decrements calculated by Kwan & Fischer to the empirical decrements measured from the 1101 spectra of 326 pre-main-sequence accretors identified in Section 3.1.2. Consistent with the chi-squared surfaces of individual sources, such as that shown in Figure 6, the fit results indicate a clear preference for a loci of models stretching from $n_{\rm H} \sim 10^{11}$ and $T = 15{,}000$ K to

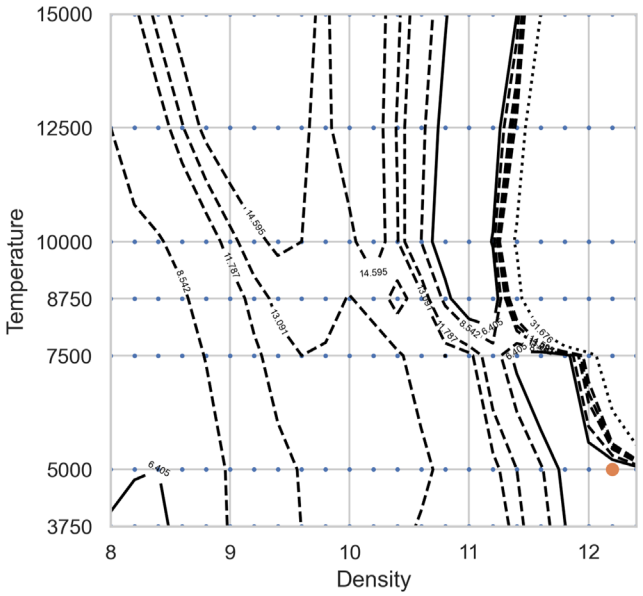

Figure 6. Visualization of the chi-squared surface for the decrement measured from the spectrum of 2M05471411+0009073 taken on MJD = 57433 (8890-57433-87). The orange dot shows the best fitted model.

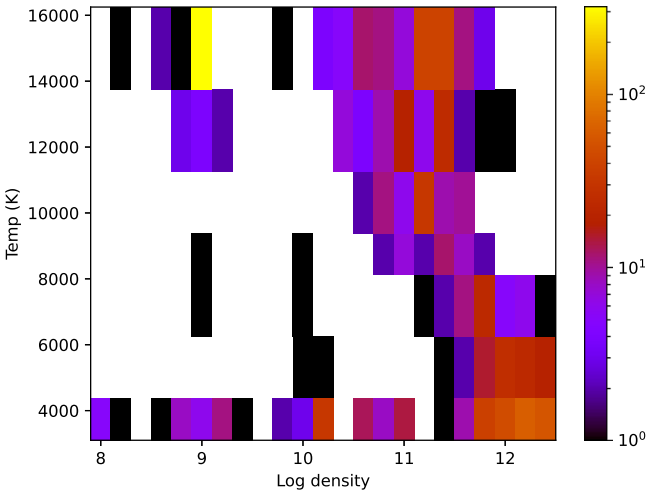

Figure 7. Distribution of model fits to 1101 spectra of 326 pre-main-sequence accretors in temperature/density space.

$n_{\rm H} \sim 10^{12.2}$ and $T = 3750$ K. This loci tracks a region of degeneracy in the Kwan & Fischer model grids, where increases in density above $n_{\rm H} \sim 10^9$ result in mid-decrement lines, such as Br15, strengthening relative to Br11, while increases in temperature cause the same mid-decrement lines to weaken. As a result, changes in the morphology of the decrement are, to first order, degenerate between anticorrelated changes in temperature and density: relative to a model with $n_{\rm H}$ 10^{11} and $T = 10{,}000$ K, a similar fit quality will be achieved by a model with somewhat higher density and somewhat lower temperature, allowing the competing influences on the resultant decrement morphology to roughly cancel out. Possibly due in part to the presence of this degeneracy, the best-fit results of the decrement fits span the full range of temperatures sampled in the Kwan & Fischer model grid, providing no clear indication of the typical temperature structure of pre-main-sequence accretion flows, or at least those that produce prominent higher-order Brackett emission lines.

The fit results do, however, clearly rule out most low-density flows; indeed, the only density lower than $n_{\rm H} \sim 10^{10}$ that is favored by a number of best-fit models is the grid point associated with $n_{\rm H} \sim 10^9$ and $T = 15{,}000$ K. This set of model parameters represents the edge of the grid in decrement space, where the strengths of mid-level Brackett lines (e.g., Br15) decline most significantly relative to the strength of Br11. As a result, any empirical decrement where the line strengths drop off more steeply than the Kwan & Fischer models suggest will find their best fit with this theoretical decrement, even if the fit is not particularly good in a global sense. We therefore interpret the 299 sources whose best-fit properties correspond to this grid point as likely spurious in nature, indicating a set of conditions, or potentially viewing angles, etc, which do not correspond well to a single-parameter solution as required by this current grid comparison.

4. Discussion

4.1. Accretion Physics

Observational support for the magnetospheric accretion model has increased significantly over the past three decades, but the initial theoretical calculations underpinning the paradigm remain quite relevant today. Hartmann et al. (1994) provided the first detailed models of the physical properties of magnetospheric accretion streams, predicting electron densities of $n_e \sim 10^{10}$–10^{12} and temperatures of 5500–7000 K along streamlines connecting the surface of a typical 0.5 $M_\odot$ T Tauri star to its circumstellar disk. These models predict that the electron densities, and the densities of bound hydrogen atoms in the second excited state, should steadily increase along each streamline as the accreting material approaches the stellar surface. Due to the enhanced efficiency of radiative cooling mechanisms at higher densities, however, the temperature predicted along each streamline does not increase monotonically, but instead rises quickly from 5500 to 7500 K shortly after the streamline departs the stellar disk, and then slowly decreases back to 7000 K as the streamline approaches the stellar surface. As a result, these models suggest material in magnetospheric accretion columns should exhibit characteristic densities of $n_e \sim 10^{10}$–10^{12}, with higher-opacity line tracers preferentially sampling lower densities further out in the streamline, and lower-opacity tracers sampling higher densities and a narrower range of excitation temperatures close to 7500 K.

Subsequent works have explored the complexity of the geometry and radiative processes in accretion flows, but have not fundamentally revised the temperature and density structures assumed in theoretical models. Calvet & Gullbring (1998) described the structure of the accretion shock and post-shock regions implied by these models, while Muzerolle et al. (2001) provided improved calculations of the emergent line emission, and identified that the maximum temperature consistent with observed line profiles appears to be inversely correlated with accretion rate (i.e., $T_{\rm max} > 10^4 K$ is allowed for accretion rates of $\dot{M} < 10^{-9} M_\odot$ yr^{-1}, but $T_{\rm max} > 7000$ K is prohibited for $\dot{M} \gtrsim 10^{-7} M_\odot$ yr^{-1}; see their Figure 16). Computational advances have also allowed significantly more complex radiative transfer methods to compute emergent line profiles (see, e.g., Kurosawa et al. 2011; Esau et al. 2014;

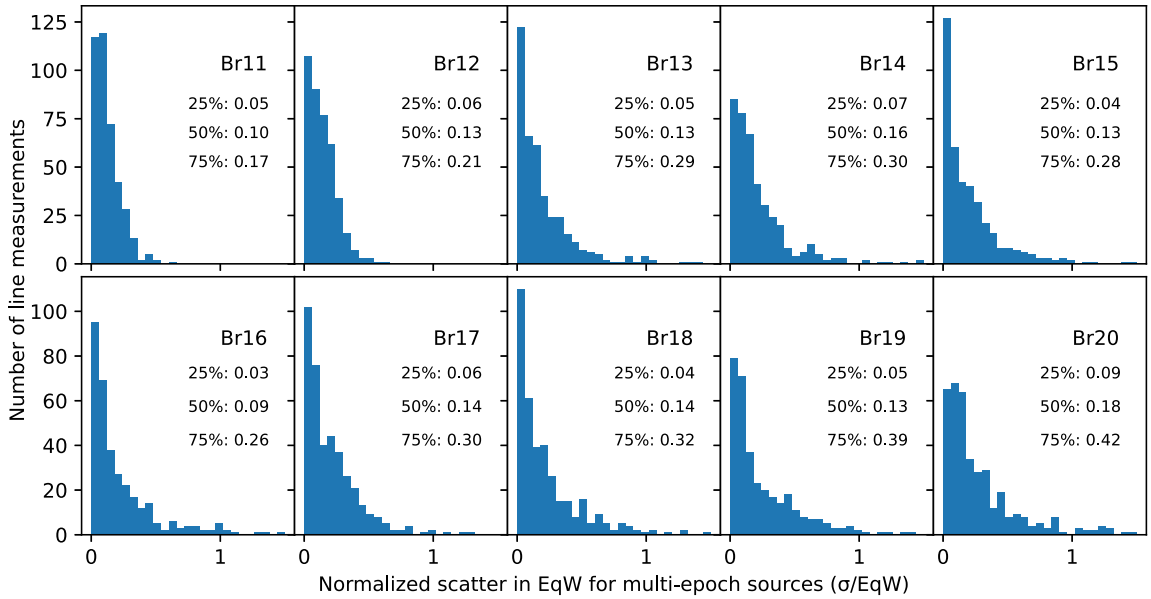

Figure 8. Histogram showing the scatter of the Brackett line strengths measured for sources with multiple spectra taken over time, relative to their mean measured line strengths: 25th, 50th, and 75th percentiles of the distribution are included in each panel, and indicate most Brackett emission lines vary by only 10%–20% on timescales of months to years. Some sources exhibit variations as large as 100%, though more frequently in the higher-order lines whose lower absolute strengths lead to larger fractional variations at fixed signal-to-noise.

Dmitriev et al. 2019; Wilson et al. 2022), and point to more complex geometries than implied in a simple dipole model (e.g., Romanova et al. 2003, 2008; Ingleby et al. 2013). Nonetheless, the formalism used by Hartmann et al. (1994) and Muzerolle et al. (2001) appears sufficient to describe the density and temperature structure of the accreting material in even nondipolar flows and provides significant explanatory power for modern observations. The 3D numerical model computed by Esau et al. (2014) for AA Tau, for example, predicts that the density of the accretion flow increases by two orders of magnitude from the circumstellar disk to the stellar surface, while producing a hot spot on the stellar surface of 5500 K.

Given the stability in the temperatures and densities expected to dominate the emission-line regions of magnetospheric accretion columns, the densities we infer from our Brackett decrement observations can be compared to those measured by a suite of complementary analyses based upon the Kwan & Fischer (2011) grid. Edwards et al. (2013) modeled Paschen decrements observed for a representative sample of CTTSs, finding best-fit densities of $n_{\rm H} \sim 10^{11}$. Rigliaco et al. (2015) infer similar densities of $n_{\rm H} \lesssim 10^{11}$ from ratios of mid-IR Pfund H I lines measured from Spitzer spectra of CTTSs and transition disk sources. With the broad optical and IR coverage offered by X-Shooter spectra, Antoniucci et al. (2017) model Balmer and Paschen decrements for CTTSs spanning a range of accretion rates, finding best-fit densities of $n_{\rm H} > 10^{11}$ for their highest-accretion-rate sources, but lower densities ($n_{\rm H} > 10^{9.6}$) for sources with lower accretion rates and/or for fits to the higher-opacity Balmer decrements. The range of tracers and accretion rates sampled by Antoniucci et al. (2017) demonstrate that higher-optical-depth tracers sample gas from a broader region of the magnetosphere, including lower-density gas that resides higher up in the accretion column.

The higher densities ($n_e > 10^{11}$) favored by our decrement fits, as well as the relative paucity of Brackett line detections among the optically selected strong accretors from the Manzo-Martínez et al. (2020; see Figure 8) sample, can both be understood as the result of optical depth effects predicted by the Kwan & Fischer (2011) model grid. The Kwan & Fischer (2011) calculations indicate that the upper-level Brackett lines become optically thick at densities of log $n_{\rm H} \sim 11$ (see, e.g., the optical thickness of Paschen beta in Figure 11 of Kwan & Fischer 2011, or the Case II model data files on Will Fischer's website)[21]. At densities greater than 10^{11}, the models predict a rapid increase in the relative strength of the higher-order Brackett lines, particularly in cases where the excitation temperatures are 8750 K or larger. In this regime, the Br11 line is predicted to become comparable in strength to the Br gamma (hereafter, BrG) line, and for the highest densities and temperatures, Br11 will become notably stronger (i.e., Br11 will be twice as strong as BrG for $T = 10{,}000$ K and log $n_{\rm H} = 12$).

A similar dynamic explains the relatively poor overlap between our sample and the Hα-selected accretors identified by Manzo-Martínez et al. (2020). At low densities, Hα is predicted to be 10^2–10^4 stronger than both BrG and Br11 (e.g., for log $n_{\rm H} = 9.0$ and $T = 8750$ K, Hα is predicted to be 2000× stronger than BrG and 13,000× stronger than Br11). As the density increases, however, the ratio drops significantly: at log $n_{\rm H} = 11$ and $T = 8750$ K, Hα is predicted to only be 47 and 60 times stronger than BrG and Br11. At log $n_{\rm H} = 12$ and $T = 8750$ K, the ratios have dropped to 12.5 and 6.5, respectively (and the Br11 line has indeed become stronger than BrG). These energetics arguments suggest that physical properties of the accretion streams, and their densities in particular, may be the primary factor determining whether the high-accretion-rate sources detected by Manzo-Martinez et al. have detectable Brackett lines or not. That is, the five-sixths of the Hα-selected sources that have no detectable Brackett lines may have characteristic accretion stream densities below 10^{11}, such that their optical emission lines are easily detected but their higher-order Brackett lines remain undetectable. The

[21] https://www.stsci.edu/~wfischer/line_models.html

remaining sixth of sources, which have strong Brackett lines as well as strong Hα emission, would then be those sources whose accretion streams have characteristic densities in excess of 10^{11}. In this interpretation, the one-sixth to five-sixths ratio of Brackett detections in the optically selected sample would reflect the relative frequency of accretion streams with densities above and below 10^{11}. Likewise, the consistent finding of densities at or above 10^{11} from most sources with secure Brackett detections would similarly support the picture in which Brackett lines will only become detectable once densities exceed the 10^{11} threshold and the lines become optically thick.

Finally, similar threshold effects could well explain the range of characteristic densities identified in accretion studies using different tracers. In each case, the mean characteristic density would likely be near, but somewhat above, the density threshold that corresponds to the transition to the line being optically thick.

4.2. Intrinsic Variability

Some YSOs were observed multiple times on different days, where each observation is called an epoch. We analyze the variability in the measurements of YSOs at different epochs to ensure confidence in the EqW measurements. If the EqW measurement of one YSO varies considerably, the model may fit the YSO to widely different density and temperatures for different epochs. Figure 8 shows how much the different epochs of the Br 11–20 lines for each YSO varies. Each data point represents one YSO. The bins are the standard deviation of the different EqW measurements of one YSO normalized by the average EqW of that Brackett line of that YSO. We see that the majority of the Brackett lines of the objects with multiple epochs vary by 10%–20% of the average EqW of the Brackett line for that object. This means the EqW measurements of different epochs of a YSO vary relatively little, and therefore we can have confidence in the model fits of the different epochs of the same object.

5. Conclusions

In this paper we present an analysis of the Brackett emission lines in the APOGEE spectra of young stars.

1. Using an automated pipeline that integrates the flux over a predefined spectral window, we identify Br11 emission lines in 9733 spectra of 4255 sources in the APOGEE DR17 data set. For each of these sources, we measure and report in a machine-readable table, whose columns are documented in Table 2, EqWs and errors for the full set of Br11–Br20 emission lines that fall within the reach of the APOGEE detectors.
2. While there is some contamination in the above selection, we perform a manual classification and EqW measurement of a subset of these Brackett emission-line sources, and train a neural network to more robustly verify the presence of the line, as well as to classify double-peaked line profiles, which are likely to be Be stars. We also identify sources with narrow lines that are more likely to be consistent with the nebular emission.
3. Restricting our sample to sources with strong, single-peaked Br11 lines, and even further to plates specifically targeting known star-forming regions and young clusters, we identify 1101 spectra of 326 likely pre-main-sequence accretors.
4. For each of the 1101 spectra of likely pre-main-sequence accretors, we calculate empirical Brackett decrements and fit them with the the radiative transfer models computed by Kwan & Fischer (2011). For nearly a third of these spectra (320 out of 1101), we measure steeper decrements (i.e., with stronger Br11 and weaker higher-order lines) than predicted by any model in the current grid. For these spectra, the closest matching predicted decrement in the model grid typically corresponds to a density $n_{\rm H} = 10^9\,{\rm cm}^{-3}$ and temperature $T = 15{,}000$ K. The remaining 781 spectra with shallower decrements (that do fall within the bounds of the model grid) show a clear preference for typical densities of 10^{11}–$10^{12}\,{\rm cm}^{-3}$. Temperatures are less well constrained, but there is a slight preference for fits with temperatures in the range 8000–15,000 K, particularly for spectra with densities near $10^{11}\,{\rm cm}^{-3}$.
5. The densities indicated by these best fits appear consistent with predictions of accretion stream models (Hartmann et al. 1994; Muzerolle et al. 2001; Dmitriev et al. 2019) and other observational studies that compare hydrogen line strengths to predictions of the Kwan & Fischer (2011) grid to infer densities of accretion columns (e.g., Edwards et al. 2013; Rigliaco et al. 2015; Antoniucci et al. 2017). Taken together, these studies support a picture where the density increases along typical CTTS accretion streams from $n_{\rm H} \sim 10^{9.6}$ (as indicated by the highest-opacity Balmer decrements; Antoniucci et al. 2017) to $n_{\rm H} \sim 10^{11}$ (as traced by the higher-opacity Paschen and Pfund lines; Edwards et al. 2013; Rigliaco et al. 2015; Antoniucci et al. 2017), and reach values as high as $n_{\rm H} \sim 10^{12}$ for the densest regions of the most heavily accreting systems, as revealed by the lowest-opacity Brackett decrements reported here.
6. Brackett line strengths measured for sources with more than one APOGEE spectrum indicate that typical epoch-to-epoch variations are no larger than 10%–20%, at or below the level of our typical measurement errors.
7. The multiplex capacity of the APOGEE spectrograph and the operational efficiency of the SDSS observing systems were critical for obtaining the observational data set that enabled the construction of this catalog of hydrogen emission-line decrements, one of the largest assembled for pre-main-sequence stars and protostars. SDSS-V has already begun observations of an even larger sample of 100,000 young stars, many of which are expected to show strong accretion signatures. With increased flexibility to co-observe with the APOGEE and BOSS spectrographs, SDSS-IV will obtain both optical and NIR spectra of these young stars, enabling at least partial coverage of the Brackett, Balmer, and Paschen series, as well as the calcium *H&K* and IR triplets. Building on the analysis presented here, measurements of the line strengths and profiles captured in this rich observational data set will enable improved constraints on the properties of accretion flows in pre-main-sequence stars.

We thank John Kwan and Will Fischer for their work to calculate and distribute the line ratio predictions that made this analysis possible. We also thank the anonymous referee for a prompt and useful report which improved the analysis presented here. H.C. and E.K. acknowledge support provided by Chandra Award Number GO9-20006X issued by the

Chandra X-ray Center, which is operated by the Smithsonian Astrophysical Observatory for and on behalf of the National Aeronautics Space Administration under contract NAS8-03060.

M.K. and K.R.C. acknowledge support provided by the NSF through grant No. AST-1449476, and from the Research Corporation via a Time Domain Astrophysics Scialog award (#24217).

C.R.Z. acknowledges support from projects UNAM-DGAPA-PAPIIT 112620 and CONACYT CB2018 A1-S-9754, Mexico.

K.P.R. acknowledges support from ANID FONDECYT Iniciación 11201161.

A.S. gratefully acknowledges support by the Fondecyt Regular (project code 1220610), and ANID BASAL projects ACE210002 and FB210003.

Funding for the Sloan Digital Sky Survey IV has been provided by the Alfred P. Sloan Foundation, the U.S. Department of Energy Office of Science, and the Participating Institutions. SDSS-IV acknowledges support and resources from the Center for High-Performance Computing at the University of Utah. The SDSS website is www.sdss.org. SDSS-IV is managed by the Astrophysical Research Consortium for the Participating Institutions of the SDSS Collaboration including the Brazilian Participation Group, the Carnegie Institution for Science, Carnegie Mellon University, the Chilean Participation Group, the French Participation Group, Harvard-Smithsonian Center for Astrophysics, Instituto de Astrofísica de Canarias, The Johns Hopkins University, Kavli Institute for the Physics and Mathematics of the Universe (IPMU)/University of Tokyo, Lawrence Berkeley National Laboratory, Leibniz Institut für Astrophysik Potsdam (AIP), Max-Planck-Institut für Astronomie (MPIA Heidelberg), Max-Planck-Institut für Astrophysik (MPA Garching), Max-Planck-Institut für Extraterrestrische Physik (MPE), National Astronomical Observatories of China, New Mexico State University, New York University, University of Notre Dame, Observatário Nacional/MCTI, The Ohio State University, Pennsylvania State University, Shanghai Astronomical Observatory, United Kingdom Participation Group, Universidad Nacional Autónoma de México, University of Arizona, University of Colorado Boulder, University of Oxford, University of Portsmouth, University of Utah, University of Virginia, University of Washington, University of Wisconsin, Vanderbilt University, and Yale University. This work has made use of data from the European Space Agency (ESA) mission Gaia (https://www.cosmos.esa.int/gaia), processed by the Gaia Data Processing and Analysis Consortium (DPAC; https://www.cosmos.esa.int/web/gaia/dpac/consortium). Funding for the DPAC has been provided by national institutions, in particular the institutions participating in the Gaia Multilateral Agreement.

Appendix
Sources with [Fe II] Emission Features

In the course of this analysis, we visually identified a number of sources with prominent [Fe II] emission lines at 16790 Å (i.e., just blueward of the main Br11 emission line; Figure 9), as well as sources with emission from unidentified lines at 16782 Å and 16776 Å. The 16791 [Fe II] line is more often seen in Be stars than YSOs, and a number of these [Fe II] emission sources were previously identified in the analysis by Chojnowski et al. (2015). Given the expansion of the APOGEE data set since the Chojnowski et al. (2015) analysis, however, for completeness we list all sources for which we observe [Fe II] emission lines in the "Fe II" column of the machine-readable table of this sample whose columns are represented in Table 2.

Sources with a prominent 16781 Å emission feature with the same velocity profile as the neighboring Br11 line are listed in the table with a "1" in the Fe II column. There are 63 sources with this emission line, of which 38 are found on young cluster plates; an example of this type is shown in the upper-left panel of Figure 9.

An additional 17 sources (but only five on young cluster plates) appear to have multiple, velocity-separated 16792 Fe II lines, potentially indicating the presence of nebular emission as well as a jet. An example of this type of spectrum, which is coded as "2" in the machine-readable table, is shown in the upper-right corner of Figure 9.

Finally, another 37 sources (of which 36 are found on young cluster plates) show an emission feature near 16775 Å. Some of these sources include additional emission lines between the 16775 Å line and Br11, while others feature just relatively weak Br11 and 16775 Å lines. Examples of these types of spectra, which are coded as "3" in the machine-readable table, are shown in the bottom row of Figure 9.

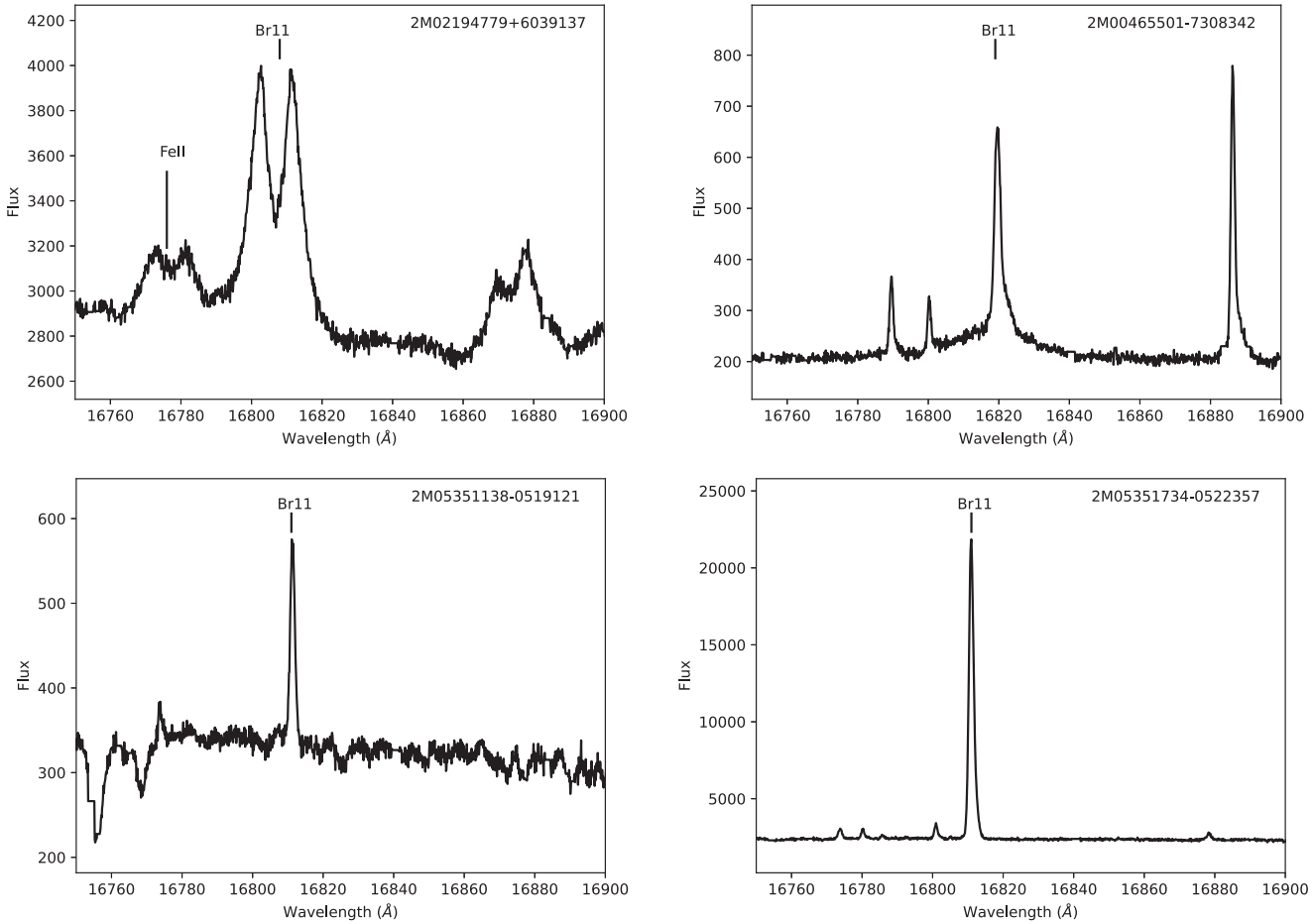

Figure 9. Top left: example of a source with (double-peaked) Br11 emission, and a neighboring 16781 Å line with an identical velocity profile. These sources are coded with an Fe II flag = 1 in the machine-readable table of our sample. Top right: example of a source with strong Br11 emission, and two lines near the wavelength expected for the neighboring [Fe II] line. These sources are coded with an Fe II flag = 2 in the machine-readable table of our sample. Bottom panels: examples of two sources with a prominent emission feature at 16775 Å: the source on the left shows this line near two photospheric features, while the source on the right shows two additional emission lines in between the 16775 Å line and Br11. Both of these patterns which include the 16775 Å feature are coded with an Fe II flag = 3 in the machine-readable table of our sample.

Table 2
Line Measurements for APOGEE DR17 Br11 Emitters

Column	Unit	Description
2MASS ID		2MASS source ID
Plate		SDSS plate ID
MJD		MJD of SDSS observation
Fiber		SDSS fiber ID
RA	deg	R.A. in J2000
Dec	deg	decl. in J2000
Telescope		SDSS telescope ID
Location		SDSS location ID
Field		SDSS field ID
Br11 auto EqW	Angstroms	Scripted equivalent width measurement of Br11 emission line
Br11 auto error	Angstroms	Uncertainty in scripted equivalent width measurement of Br11 emission line
Br12 auto EqW	Angstroms	Scripted equivalent width measurement of Br12 emission line
Br12 auto error	Angstroms	Uncertainty in scripted equivalent width measurement of Br12 emission line
Br13 auto EqW	Angstroms	Scripted equivalent width measurement of Br13 emission line
Br13 auto error	Angstroms	Uncertainty in scripted equivalent width measurement of Br13 emission line
Br14 auto EqW	Angstroms	Scripted equivalent width measurement of Br14 emission line
Br14 auto error	Angstroms	Uncertainty in scripted equivalent width measurement of Br14 emission line
Br15 auto EqW	Angstroms	Scripted equivalent width measurement of Br15 emission line
Br15 auto error	Angstroms	Uncertainty in scripted equivalent width measurement of Br15 emission line
Br16 auto EqW	Angstroms	Scripted equivalent width measurement of Br16 emission line
Br16 auto error	Angstroms	Uncertainty in scripted equivalent width measurement of Br16 emission line
Br17 auto EqW	Angstroms	Scripted equivalent width measurement of Br17 emission line

Table 2
(Continued)

Column	Unit	Description
Br17 auto error	Angstroms	Uncertainty in scripted equivalent width measurement of Br17 emission line
Br18 auto EqW	Angstroms	Scripted equivalent width measurement of Br18 emission line
Br18 auto error	Angstroms	Uncertainty in scripted equivalent width measurement of Br18 emission line
Br19 auto EqW	Angstroms	Scripted equivalent width measurement of Br19 emission line
Br19 auto error	Angstroms	Uncertainty in scripted equivalent width measurement of Br19 emission line
Br20 auto EqW	Angstroms	Scripted equivalent width measurement of Br20 emission line
Br20 auto error	Angstroms	Uncertainty in scripted equivalent width measurement of Br20 emission line
YC object		Flag indicating a source is in the young cluster sample (= 1 if so, 0 if not)
YC density	n_e cm^{-3}	Electron density of best-fit model to brackett decrement (for sources on young cluster plates)
YC max. dens.	n_e cm^{-3}	Maximum electron density of models within 2.3 of minimum chi square (for sources on young cluster plates)
YC min. dens.	n_e cm^{-3}	Minimum electron density of models within 2.3 of minimum chi square (for sources on young cluster plates)
YC dens. std. dev.	n_e cm^{-3}	Standard deviation of electron densities for models within 2.3 of minimum chi square (for sources on young cluster plates)
YC temp.	deg (K)	Gas temperature of best-fit model to brackett decrement (for sources on young cluster plates)
YC max. temp.	deg (K)	Maximum gas temperature of all models within 2.3 of minimum chi square (for sources on young cluster plates)
YC min. temp.	deg (K)	Minimum gas temperature of all models within 2.3 of minimum chi square (for sources on young cluster plates)
YC temp. std. dev.	deg (K)	Standard deviation of gas temperature for all models within 2.3 of minimum chi square (for sources on young cluster plates)
YC chi		Chi square of best-fit model to brackett decrement (for sources on young cluster plates)
YC chi dev.		Standard deviation of chi square values for fits within 2.3 of minimum chi square (for sources on young cluster plates)
Slope		ratio of continuum fluxes near the Br11 and Br20 lines, presented as $\mathrm{Br11}_{cont}\,\mathrm{Br20}_{cont}$ (values greater than 1 represent sources with SEDs rising to long wavelengths)
Fe II		Fe II emission flag; 1 if one Fe II line detected; 2 if two velocity-separated Fe II lines detected; 0 otherwise
NN detected		Neural net classification for Br line detection (1 = line detected; 0 = no line detected)
NN double		Neural net classification of Br line profiles (1 = double peaked profile; 0 = single peak profile)
NN nebular		Neural net classification for br line width (1 = narrow/ISM width; 0 = doppler broadened profile)
NN good		Neural net classification of Br line quality (1 = good; 0 = bad)
NN center vel.	km s^{-1}	Neural net estimate of Br line center velocities
NN vel. scatter	km s^{-1}	Neural net estimate of uncertainty in Br line center velocities
NN vel. width	km s^{-1}	Neural net estimate of velocity width of Br line profiles
NN vel. width scatter	km s^{-1}	Neural net estimate of uncertainty in Br line velocity width
NN maxline		Highest order brackett line detected by the neural net analysis
Br11 NN EqW	Angstroms	Neural net equivalent width measurement of Br11 emission line
Br11 NN error	Angstroms	Uncertainty in neural net equivalent width measurement of Br11 emission line
Br12 NN EqW	Angstroms	Neural net equivalent width measurement of Br12 emission line
Br12 NN error	Angstroms	Uncertainty in neural net equivalent width measurement of Br12 emission line
Br13 NN EqW	Angstroms	Neural net equivalent width measurement of Br13 emission line
Br13 NN error	Angstroms	Uncertainty in neural net equivalent width measurement of Br13 emission line
Br14 NN EqW	Angstroms	Neural net equivalent width measurement of Br14 emission line
Br14 NN error	Angstroms	Uncertainty in neural net equivalent width measurement of Br14 emission line
Br15 NN EqW	Angstroms	Neural net equivalent width measurement of Br15 emission line
Br15 NN error	Angstroms	Uncertainty in neural net equivalent width measurement of Br15 emission line
Br16 NN EqW	Angstroms	Neural net equivalent width measurement of Br16 emission line
Br16 NN error	Angstroms	Uncertainty in neural net equivalent width measurement of Br16 emission line
Br17 NN EqW	Angstroms	Neural net equivalent width measurement of Br17 emission line
Br17 NN error	Angstroms	Uncertainty in neural net equivalent width measurement of Br17 emission line
Br18 NN EqW	Angstroms	Neural net equivalent width measurement of Br18 emission line
Br18 NN error	Angstroms	Uncertainty in neural net equivalent width measurement of Br18 emission line
Br19 NN EqW	Angstroms	Neural net equivalent width measurement of Br19 emission line
Br19 NN error	Angstroms	Uncertainty in neural net equivalent width measurement of Br19 emission line
Br20 NN EqW	Angstroms	Neural net equivalent width measurement of Br20 emission line
Br20 NN error	Angstroms	Uncertainty in neural net equivalent width measurement of Br20 emission line

(This table is available in its entirety in machine-readable form.)

ORCID iDs

Hunter Campbell https://orcid.org/0000-0001-5436-5388
Elliott Khilfeh https://orcid.org/0000-0001-9649-6028
Kevin R. Covey https://orcid.org/0000-0001-6914-7797
Marina Kounkel https://orcid.org/0000-0002-5365-1267
Carlos G. Román-Zúñiga https://orcid.org/0000-0001-8600-4798
Jesús Hernández https://orcid.org/0000-0001-9797-5661
Ezequiel Manzo Martínez https://orcid.org/0000-0001-6647-862X
Karla Peña Ramírez https://orcid.org/0000-0002-5855-401X
Alexandre Roman-Lopes https://orcid.org/0000-0002-1379-4204
Keivan G. Stassun https://orcid.org/0000-0002-3481-9052
Guy S. Stringfellow https://orcid.org/0000-0003-1479-3059
Jura Borissova https://orcid.org/0000-0002-5936-7718
S. Drew Chojnowski https://orcid.org/0000-0001-9984-0891
Valeria Ramírez-Preciado https://orcid.org/0000-0002-4013-2716
Jinyoung Serena Kim https://orcid.org/0000-0001-6072-9344
Javier Serna https://orcid.org/0000-0001-7351-6540
Amelia M. Stutz https://orcid.org/0000-0003-2300-8200
Ricardo López-Valdivia https://orcid.org/0000-0002-7795-0018
Genaro Suárez https://orcid.org/0000-0002-2011-4924
Jason E. Ybarra https://orcid.org/0000-0002-3576-4508
Penélope Longa-Peña https://orcid.org/0000-0001-9330-5003
José G. Fernández-Trincado https://orcid.org/00000-0003-3526-5052

References

Abadi, M., Agarwal, A., Barham, P., et al. 2015, TensorFlow: Large-Scale Machine Learning on Heterogeneous Systems, https://www.tensorflow.org/
Abdurro'uf, Accetta, K., Aerts, C., et al. 2022, ApJS, 259, 35
Antoniucci, S., Nisini, B., Giannini, T., et al. 2017, A&A, 599, A105
Bae, J., Hartmann, L., Zhu, Z., & Nelson, R. P. 2014, ApJ, 795, 61
Baker, J. G., & Menzel, D. H. 1938, ApJ, 88, 52
Beaton, R. L., Oelkers, R. J., Hayes, C. R., et al. 2021, AJ, 162, 302
Blanton, M. R., Bershady, M. A., Abolfathi, B., et al. 2017, AJ, 154, 28
Borissova, J., Roman-Lopes, A., Covey, K., et al. 2019, AJ, 158, 46
Calvet, N., & Gullbring, E. 1998, ApJ, 509, 802
Cañas, C. I., Bender, C. F., Mahadevan, S., et al. 2018, ApJL, 861, L4
Chojnowski, S. D., Whelan, D. G., Wisniewski, J. P., et al. 2015, AJ, 149, 7
Cottaar, M., Covey, K. R., Meyer, M. R., et al. 2014, ApJ, 794, 125
Cottle, J. N., Covey, K. R., Suárez, G., et al. 2018, ApJS, 236, 27
Czesla, S., Schröter, S., Schneider, C. P., et al. 2019, PyA: Python Astronomy-related Packages, Astrophysics Source Code Library, ascl:1906.010
Da Rio, N., Tan, J. C., Covey, K. R., et al. 2016, ApJ, 818, 59
Dmitriev, D. V., Grinin, V. P., & Katysheva, N. A. 2019, AstL, 45, 371
Edwards, S., Kwan, J., Fischer, W., et al. 2013, ApJ, 778, 148
Esau, C. F., Harries, T. J., & Bouvier, J. 2014, MNRAS, 443, 1022
Foster, J. B., Cottaar, M., Covey, K. R., et al. 2015, ApJ, 799, 136
García Pérez, A. E., Allende Prieto, C., Holtzman, J. A., et al. 2016, AJ, 151, 144
Gunn, J. E., Siegmund, W. A., Mannery, E. J., et al. 2006, AJ, 131, 2332
Gutiérrez, M., Catlett, V., Tofflemire, B. M., Mace, G., & Kraus, A. L. 2020, RNAAS, 4, 7
Hartmann, L., Herczeg, G., & Calvet, N. 2016, ARA&A, 54, 135
Hartmann, L., Hewett, R., & Calvet, N. 1994, ApJ, 426, 669
Holtzman, J. A., Shetrone, M., Johnson, J. A., et al. 2015, AJ, 150, 148
Hummer, D. G., & Storey, P. J. 1987, MNRAS, 224, 801
Ingleby, L., Calvet, N., Herczeg, G., et al. 2013, ApJ, 767, 112
Jönsson, H., Holtzman, J. A., Allende Prieto, C., et al. 2020, AJ, 160, 120
Kounkel, M., Covey, K., Suárez, G., et al. 2018, AJ, 156, 84
Kurosawa, R., Romanova, M. M., & Harries, T. J. 2011, MNRAS, 416, 2623
Kwan, J., & Fischer, W. 2011, MNRAS, 411, 2383
Majewski, S. R., Schiavon, R. P., Frinchaboy, P. M., et al. 2017, AJ, 154, 94
Manzo-Martínez, E., Calvet, N., Hernández, J., et al. 2020, ApJ, 893, 56
Medina, N., Borissova, J., Kurtev, R., et al. 2021, ApJ, 914, 28
Muzerolle, J., Calvet, N., & Hartmann, L. 2001, ApJ, 550, 944
Nidever, D. L., Holtzman, J. A., Allende Prieto, C., et al. 2015, AJ, 150, 173
Piskunov, N. E., & Valenti, J. A. 2002, A&A, 385, 1095
Rigliaco, E., Pascucci, I., Duchene, G., et al. 2015, ApJ, 801, 31
Roman-Lopes, A., Román-Zúñiga, C. G., Tapia, M., Minniti, D., & Borissova, J. 2020, ApJS, 247, 17
Román-Zúñiga, C. G., Kounkel, M., Hernández, J., et al. 2022, arXiv:2211.09217
Romanova, M. M., Kulkarni, A. K., & Lovelace, R. V. E. 2008, ApJL, 673, L171
Romanova, M. M., Ustyugova, G. V., Koldoba, A. V., Wick, J. V., & Lovelace, R. V. E. 2003, ApJ, 595, 1009
Santana, F. A., Beaton, R. L., Covey, K. R., et al. 2021, AJ, 162, 303
Vollmann, K., & Eversberg, T. 2006, AN, 327, 862
White, R. J., & Basri, G. 2003, ApJ, 582, 1109
Wilson, J. C., Hearty, F. R., Skrutskie, M. F., et al. 2019, PASP, 131, 055001
Wilson, T. J. G., Matt, S., Harries, T. J., & Herczeg, G. J. 2022, MNRAS, 514, 2162
Zasowski, G., Cohen, R. E., Chojnowski, S. D., et al. 2017, AJ, 154, 198
Zasowski, G., Johnson, J. A., Frinchaboy, P. M., et al. 2013, AJ, 146, 81